Paper

Anodic Dissolution Behavior of Al Alloys Containing Al_6Fe or β-AlFeSi in EmImCl–$AlCl_3$ Electrolyte during Electrorefining*

Junji Nunomura**, Hisayoshi Matsushima***, Yoshihiko Kyo**,
Yoichi Kojima**** and Mikito Ueda*****

To produce over 99.9% of high-purity Al from Al alloys containing Al_6Fe or β-AlFeSi through electrorefining, their anodic dissolution and cathodic electrodeposition characteristics should be clarified. In this study, the anodic dissolution and cathodic electrodeposition behavior of Al–Fe binary and Al–Fe–Si ternary alloys were investigated in an EmImCl–$AlCl_3$ ionic liquid electrolyte at 323 K. Anodic polarization measurements, constant potential electrolysis, X-ray diffraction (XRD), scanning electron microscopy (SEM), field-emission SEM (FE-SEM), and energy dispersive spectroscopy (EDS) were used to study the anode and electrodeposits on the cathode. Constant potential electrolysis showed that Fe dissolved from Al_6Fe in the Al–Fe anode at 0.7 V vs Al/Al(III) and from β-AlFeSi in the Al–Fe–Si anode at 1.4 V and was co-deposited with Al on the cathode. Notably, Si did not dissolve from β-AlFeSi at either potential. A combination of controlled anodic dissolution potential and the use of the Al alloy containing β-AlFeSi further suppressed the dissolution and cathodic co-deposition of Fe, affording high-purity Al on the cathode. This suggests that Al alloys with intermetallic compounds that are less likely to dissolve Fe at the anode are optimal for obtaining over 99.9% of high-purity Al from Al alloys containing Fe in the electrorefining method.

Keywords: *anodic dissolution, electrorefining, Al–Fe alloy, Al–Fe–Si alloy, metallurgical structure, ionic liquid*

1. Introduction

Aluminum (Al) is used in automobiles, building materials, and beverage cans[1)~5)]. Primary Al is produced by the Hall–Heroult process, which has a significant environmental impact because of the CO_2 emissions during smelting and high energy consumption[6)~8)]. Al has a lower melting point than metals such as Fe, and consequently, scrap Al is easily remelted and recycled[9)]. Recycled Al obtained via remelting has a low environmental impact because it is produced using less than 5% of the energy required for smelting[4), 7), 10)~12)]. Hence, Al recycling should be promoted.

Al materials are broadly classified into wrought and casting alloys. High-quality raw materials with few impurities are required for obtaining wrought alloys with excellent mechanical properties[13), 14)]. In particular, an Al–Fe intermetallic compound exhibits a significant decrease in toughness and is brittle[15)~17)]. Al–Fe alloys with high Fe content are classified as 8000 series wrought alloys; however, they have limited applications, such as in the manufacture of Al foil, and they are not as widely used as the other Al wrought alloys comprising Al as the major component[18), 19)]. In contrast, casting alloys can be manufactured using low-quality alloys containing many impurities, such as recycled Al discharged from wrought alloys[20), 21)]. Recycling with decreasing quality is called cascade recycling, which eventually yields Al

* This paper has been published in J. Electrochem. Soc., **170** (2023), 122501.

** Fundamental Research Department, Research & Development Center, Marketing & Technology Division, UACJ Corporation, Dr. Eng.
*** Faculty of Engineering, Hokkaido University, Dr. Eng.
**** Research & Development Center, Marketing & Technology Division, UACJ Corporation, Ph. D.
***** Faculty of Engineering, Hokkaido University, Ph. D.

scrap that is difficult to recycle[21), 22)]. In particular, ADC12, used in automobile engine parts, contains large amounts of Fe, Si, and Cu and has become a mainstream casting alloy manufactured from cascade recycling of scrap Al. However, the engine blocks used in conventional vehicles with internal combustion engines are the largest consumers of Al casting alloys. As electric vehicles do not have internal combustion engines, it is predicted that the use of casting alloys will be reduced in the future as electric vehicles become more widespreas[23)]. Whereas, the demand for high-quality wrought alloys is expected to increase to reduce the weight of automobiles[13), 14), 23)]. Therefore, to promote recycling, the effective use of Fe-rich scrap Al is essential. Further recycling of this low-quality Al scrap can lead to a more efficient use of resources and reduce its environmental impact.

We previously reported an electrorefining method for recycling Al scrap[24)~26)]. Recycling using the electrorefining method has been reported in attempts using molten salts[27)~29)] or ionic liquids as the electrolyte[30)~34)] however we focus particularly on methods that use low temperature ionic liquids as an electrolyte. Since this method requires less energy to maintain the bath temperature, the entire process is expected to be an energy-saving electrorefining method.

Solid Al alloys are used as anodes in the low-temperature electrolyte. Moreover, as Al can form solid solutions and complex intermetallic compounds depending on the additives used and the manufacturing method, understanding the anodic dissolution behavior for these metallurgical structures is important. In this context, we previously clarified the anodic dissolution and electrorefining behavior of Al–Si[24)], Al–Cu[25)], and Al–Mn[26)] alloy anodes. In the case of the Al–Si alloy, Al dissolves preferentially over Si from the anode surface, as Si does not easily dissolve in the electrolyte, resulting in the recovery of high-purity Al on the cathode. However, in the case of the Al–Cu alloy, Al_2Cu is dissolved in the electrolyte depending on the anodic potential, which is an important parameter for recovering high-purity Al from the cathode. In the case of the Al–Mn alloy, the anodic dissolution potentials at the Mn solid solution in the matrix and at the intermetallic compound differ. Notably, the metallurgical structure of Al exhibits various anodic dissolution behaviors in ionic liquids, and thus, is another important parameter for the recovery of high-purity Al at the cathode. Therefore, understanding the anodic dissolution behavior of individual metallurgical structures is necessary to design the most suitable anodes for electrorefining; however, very few studies have focused on this issue.

As mentioned above, Fe significantly degrades the mechanical properties of wrought alloys; therefore, Al scrap containing Fe is recycled as a casting alloy. Because Fe is hardly solid-soluble in Al, binary Al–Fe intermetallic compounds, such as Al_6Fe and Al_3Fe, are formed[16), 18), 35)]. Ternary intermetallic compounds such as α-AlFeSi and β-AlFeSi are formed with Si derived from impurities in wrought alloys and from additives in casting alloys[36), 37)]. Additionally, Fe and Al are readily co-deposited on the cathode when Fe ions are present in the electrolyte[38)~40)]. To remove Fe from Al scrap, the dissolution of Fe from intermetallic compounds containing Fe in the Al alloys used as anodes should be prevented. The electrolysis conditions that prevent the dissolution of Fe and the metallurgical structures that do not easily dissolve at the anode must be clarified.

In this study, Al–Fe binary and Al–Fe–Si ternary alloys with controlled intermetallic compound types and sizes were used to investigate the anodic dissolution and cathodic electrodeposition behaviors of each alloy with respect to their metallurgical structures.

2. Experimental

Pure Fe (99.99mass%Fe [99.99%Fe], 0.3 mm thickness, Nilaco), pure Al (99.999mass%Al [99.999%Al], 0.5 mm thickness, Nilaco), Al–1.5mass%Fe (Al–1.5%Fe), and Al–1.5mass%Fe–3.5mass%Si (Al–1.5%Fe–3.5%Si) casting alloys, as well as cold-rolled plates, were used as anodes. Casting alloys (175 mm × 175 mm × 34 mm) were prepared via a semi-continuous direct-chill casting method[41)] using 99.9mass%Al as primary Al, Al–25mass%Si master alloy, and Al–10mass%Fe master alloy. Subsequently,

the samples were cut to a thickness of 30 mm and ground flat on either side using a milling machine (STM2V, Okuma & Howa Machine). Cold-rolled sheets were fabricated by heat-treating the casting alloys and subsequent rolling. The casting alloys were homogenized in an electric furnace at 773 K for Al–1.5%Fe–3.5%Si and 823 K for Al–1.5%Fe for 6 h and then hot-rolled to a thickness of 3 mm. After intermediate annealing at 623 K for 1 h , the alloy sheets were cold-rolled to a thickness of 1 mm. The compositions of the casting alloys were determined using an optical emission spectrometer (ARL4460, Thermo Fisher Scientific). At the same time, their electrical conductivities were measured using a conductivity meter (SIGMATEST 2.069, FOERSTER). The preparation of the ionic liquid and all electrochemical measurements were performed in an Ar-filled glove box (B Type PC, AS ONE) with a humidity below 5%. The ionic liquid electrolyte was obtained by mixing 1-ethyl-3-methyl imidazolium chloride (EmImCl, 96mass%, Tokyo Chemical Co., Ltd.) and anhydrous $AlCl_3$ (99.99mass%, Kishida Chemical Co., Ltd.) at a 1 : 2 molar ratio. An Al wire (99.99mass%, 1.5 mm diameter, Nippon Light Metal) was immersed to stand in the ionic liquid for more than 48 h at 323 K to remove water and impurities. Electrochemical measurements were conducted in a three-electrode cell using high-purity Fe, high-purity Al, Al–Fe, and Al–Fe–Si alloys as working electrodes, Pt and Cu plates as counter electrodes, and Al wires as reference electrodes. High-purity Fe, high-purity Al, Al–Fe, Al–Fe–Si, Al wires, and Cu plates were polished from #220 to #800 using a water-resistant polishing paper and ultrasonically cleaned with acetone. The Pt plates were polished from #220 to #400 using a water-resistant polishing paper and ultrasonically cleaned with acetone. The alloy anode was masked with a polytetrafluoroethylene sealing tape (ASF-110FR, Chuko Chemical Industries) to maintain an immersion area of 10 mm × 20 mm. The inter-electrode distance between the working and counter electrodes was 20 mm. The electrolyte was heated to 323 K using a hot plate stirrer, and each electrode was connected to a potentiostat (HZ-Pro Hokuto Denko Co., Ltd.) for anodic polarization measurements and constant-potential electrolysis. Anodic polarization measurements were obtained at an immersion potential of 1500 mV with a scanning rate of 1 mV s^{-1} after 20 min of immersion of the specimens in the ionic liquid. Constant potential electrolysis was performed at 0.4, 0.7, 0.9, and 1.4 V with an electric charge density of 100 C cm^{-2}. Subsequently, the anode specimens were rinsed with distilled water and dried. Then, they were characterized via visual observation, Xray diffraction (XRD; D2PHASER, Bruker, Cu-Kα radiation), scanning electron microscopy (SEM, JSM-6610, JEOL), and fieldemission scanning electron microscopy (FE-SEM, JSM-7200F, JEOL). Next, the cathode specimens were rinsed with distilled water and dried. Then, they were characterized via visual observation and SEM. The electrodeposits that peeled off the cathode were also collected and observed using SEM. The specimens obtained before and after constant potential electrolysis were embedded into a polyester cold resin, cut, polished from #220 to #2400 with waterresistant polishing paper, and finished to a mirror-like surface using 9 µm, 3 µm, and 1 µm diamond sprays (DP-Spray, Struers). Their cross-sections were observed by FE-SEM.

3. Results

The Al–Fe and Al–Fe–Si alloy compositions measured using optical emission spectrometry are listed in **Table 1**. The alloys contained trace impurities derived from primary Al. The electrical conductivity of the Al–Fe and Al–Fe–Si alloy compositions measured by a conductivity meter are listed in **Table 2**. The electrical conductivity of Al–Fe alloys was similar to 55.7% international annealed copper standard (IACS)[26] for casting alloy and 58.5%

Table 1 Composition of the Al–Fe and Al–Fe–Si alloy specimens.

Specimen	Composition [mass%]								
	Si	Fe	Cu	Mn	Mg	Zn	Cr	Ti	Al
Al–1.5%Fe	0.02	1.42	< 0.01	< 0.01	< 0.01	< 0.01	< 0.01	< 0.01	bal.
Al–1.5%Fe–3.5%Si	3.27	1.47	< 0.01	0.01	< 0.01	< 0.01	< 0.01	< 0.01	bal.

Table 2 The electrical conductivities of Al–Fe and Al–Fe–Si alloy specimens.

Specimen	Electric conductivity [%IACS]	
	Casting alloy	Cold-rolled plate
Al–1.5%Fe	55.7	58.5
Al–1.5%Fe–3.5%Si	39.0	51.8

IACS for cold-rolled plate, whereas electrical conductivities of Al–Fe–Si alloys was different to 39.0% IACS for casting alloy and 51.8% IACS for cold-rolled plate. The anodic polarization measurements of the 99.999%Al, 99.99%Fe, Al–1.5%Fe, and Al–1.5%Fe–3.5%Si alloys are shown in **Fig. 1**. For 99.99% Fe, the current density increased linearly from 0.54 V vs Al/Al(III). For 99.999% Al, the current density increased linearly from the natural immersion potential to 0.43 V. The current density reached a maximum value at 0.43 V, sharply decreased to a minimum value at 0.52 V, increased again to 1.08 V, and finally reached a steady-state value. However, the anodic polarization curves of the Al–1.5%Fe casting alloy and cold-rolled plate showed peaks of current density at approximately 0.7 V in addition to the dissolution behavior described above. The anodic polarization curves of Al–1.5%Fe–3.5%Si casting alloy and cold-rolled plate exhibited peaks of current density at approximately 0.9 V and 1.4 V in addition to the dissolution behavior described above.

Subsequently, constant potential electrolysis was performed to investigate the dissolution behavior of these alloys and their electrodeposition behavior on the cathode at 0.4, 0.7, and 1.4 V for the Al–1.5%Fe alloy and 0.4, 0.9, and 1.4 V for the Al–1.5%Fe–3.5%Si alloy at an electric charge density of 100 C cm^{-2}. The electric charge density vs anode current density

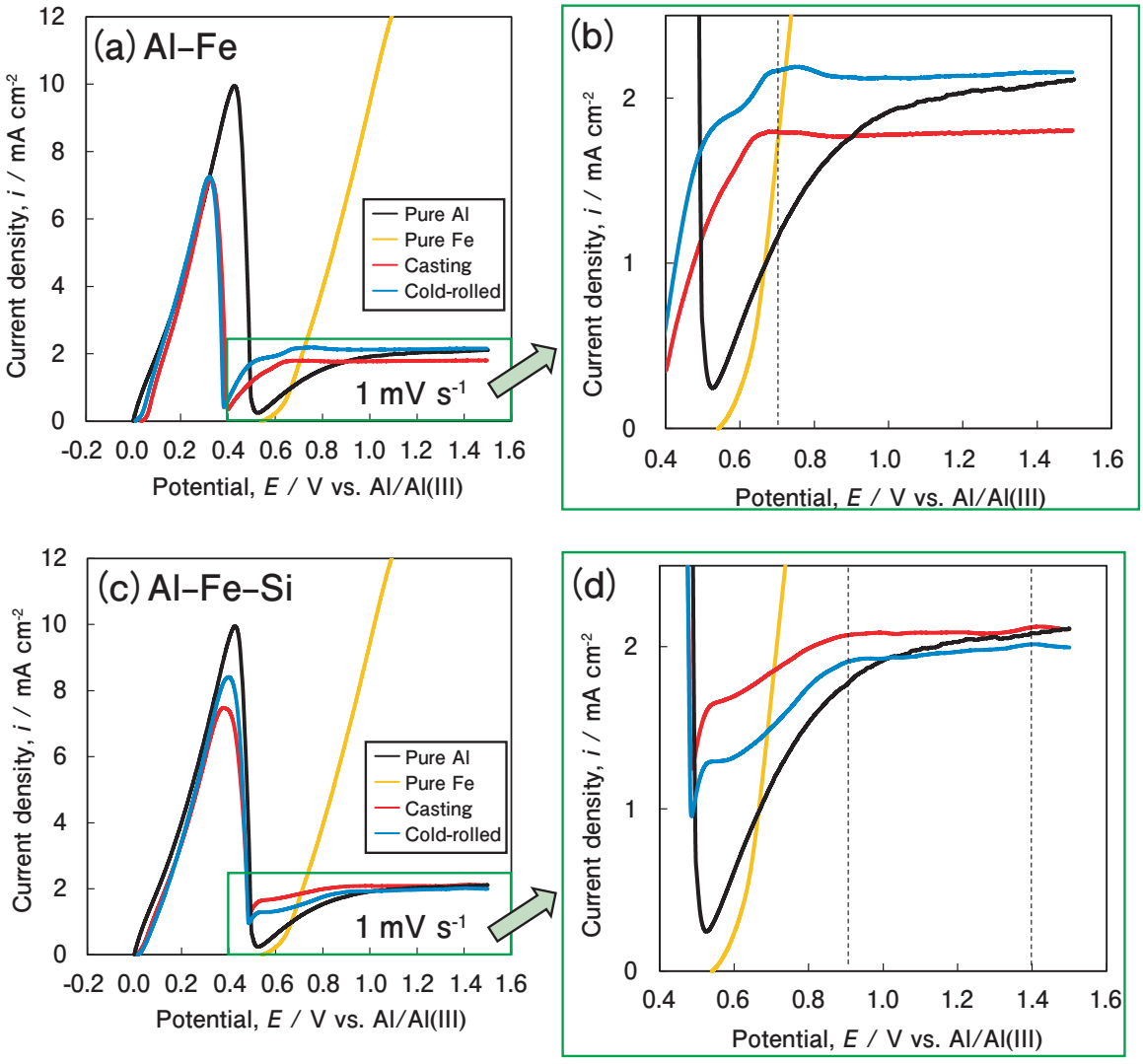

Fig. 1 Anodic polarization curves of (a)–(b) 99.99% Fe, 99.999% Al, and Al–1.5%Fe casting alloy and cold-rolled plate and those of (c)–(d) 99.99% Fe, 99.999% Al, and Al–1.5%Fe–3.5%Si alloy and cold-rolled plate in the EmImCl–$AlCl_3$ ionic liquid (1 : 2 molar ratio) at a scan rate of 1 mV s^{-1} and 323 K.

curves for constant potential electrolysis are shown in **Fig. 2**. The Al–1.5%Fe (Fig. 2 (a)) and Al–1.5%Fe–3.5%Si (Fig. 2 (c)) casting alloys showed an increase in current density at the beginning of electrolysis as the potential became more noble; however, the current density decreased as the electric charge density increased, showing a steady-state value of approximately 2 mA cm^{-2} regardless of the potential. The coldrolled plates of Al–1.5%Fe (Fig. 2 (b)) and Al–1.5%Fe–3.5%Si (Fig. 2 (d)) alloys showed an increase in the current density at the beginning of electrolysis as the potential became more noble. The current density decreased as the electric charge density increased; however, higher steady-state current densities were observed as the potential became more noble. Photographs obtained after constant potential electrolysis are shown in **Fig. 3**. The surfaces of the Al–1.5%Fe casting alloy and cold-rolled plate became dark at 0.4 V, whereas smooth surfaces were observed at 0.7 and 1.4 V. The surfaces of the Al–1.5%Fe–3.5%Si casting alloy and cold-rolled plate changed to a darker color than those of the Al–1.5%Fe alloy. In addition, the surface of the Al–1.5%Fe–3.5%Si casting alloy changed to a darker color with shading at 0.9 V, and a portion of the surface changed to a darker color at 1.4 V. The surface of the Al–1.5%Fe–3.5%Si cold-rolled plate changed to gray at 0.9 V, and a smooth surface was observed at 1.4 V.

In the XRD patterns of the Al–1.5%Fe casting alloy and coldrolled plate obtained before and after constant potential electrolysis (**Fig. 4** (a), (b)) peaks consistent with Al and Al_6Fe. were clearly observed. Moreover, in the XRD patterns of the Al–1.5%Fe–3.5%Si alloy and cold-rolled plate (Fig. 4 (c), (d)) peaks consistent with Al, β-AlFeSi, and Si were clearly

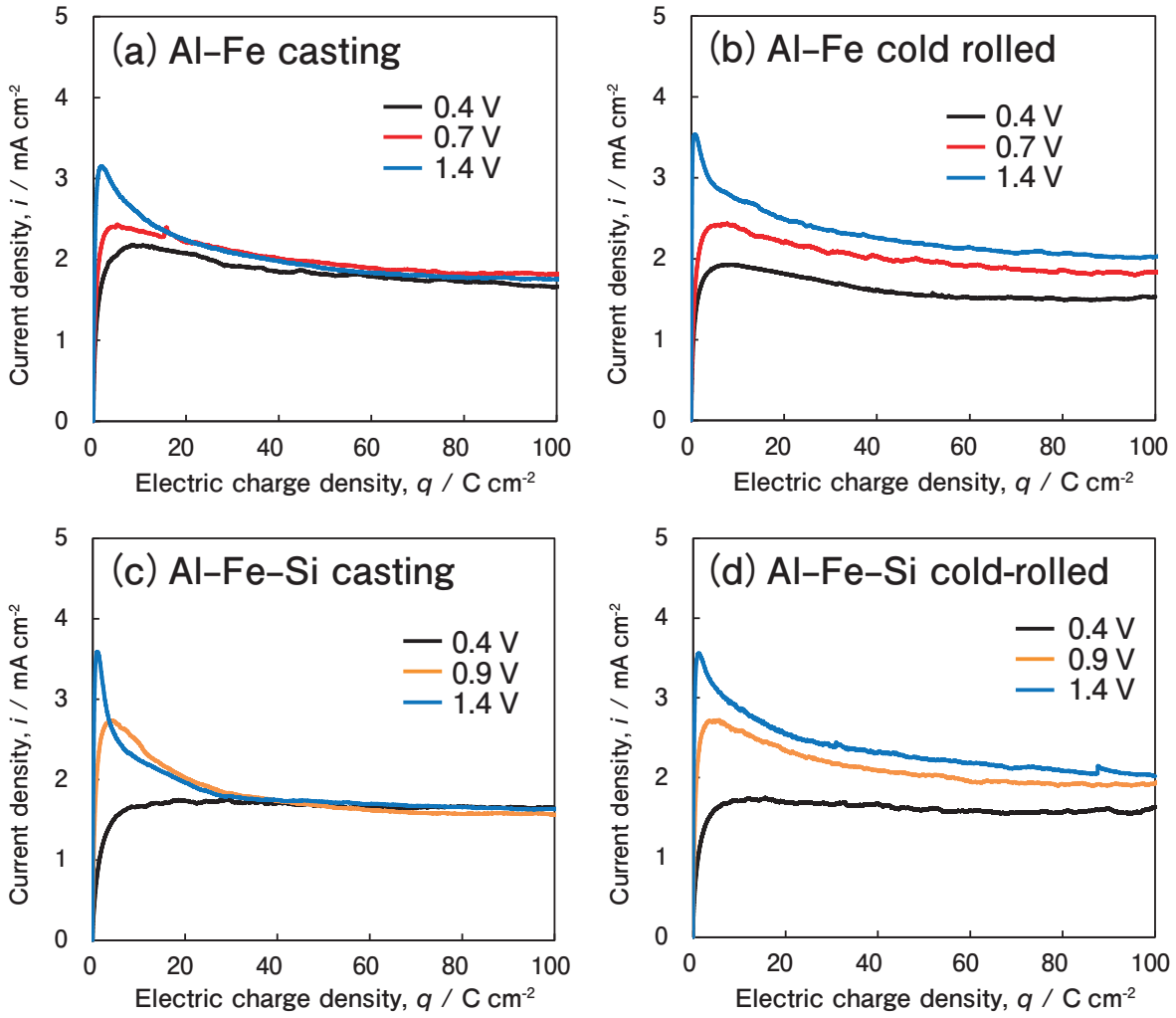

Fig. 2 Changes in the electric charge density with changing current density during constant potential electrolysis in the EmImCl–$AlCl_3$ ionic liquid for the Al–1.5%Fe (a) casting alloy and (b) cold-rolled plate and those of the Al–1.5%Fe–3.5%Si (c) casting alloy and (d) cold-rolled plate at 0.4, 0.7, 0.9, and 1.4 V, with a charge density of 100 C cm^{-2}.

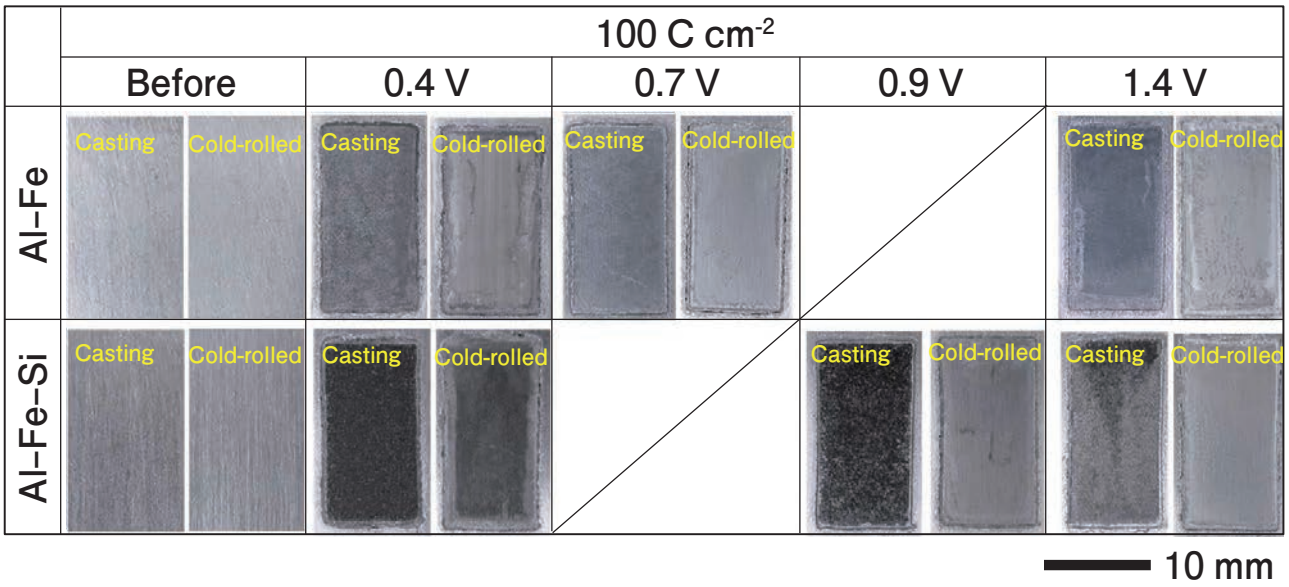

Fig. 3 Photographs of the Al–1.5%Fe and Al–15%Fe–3.5%Si casting alloy and cold-rolled plate before and after constant potential electrolysis in the EmImCl–$AlCl_3$ ionic liquid at 0.4, 0.7, 0.9, and 1.4 V, with a charge density of 100 C cm^{-2} at 323 K.

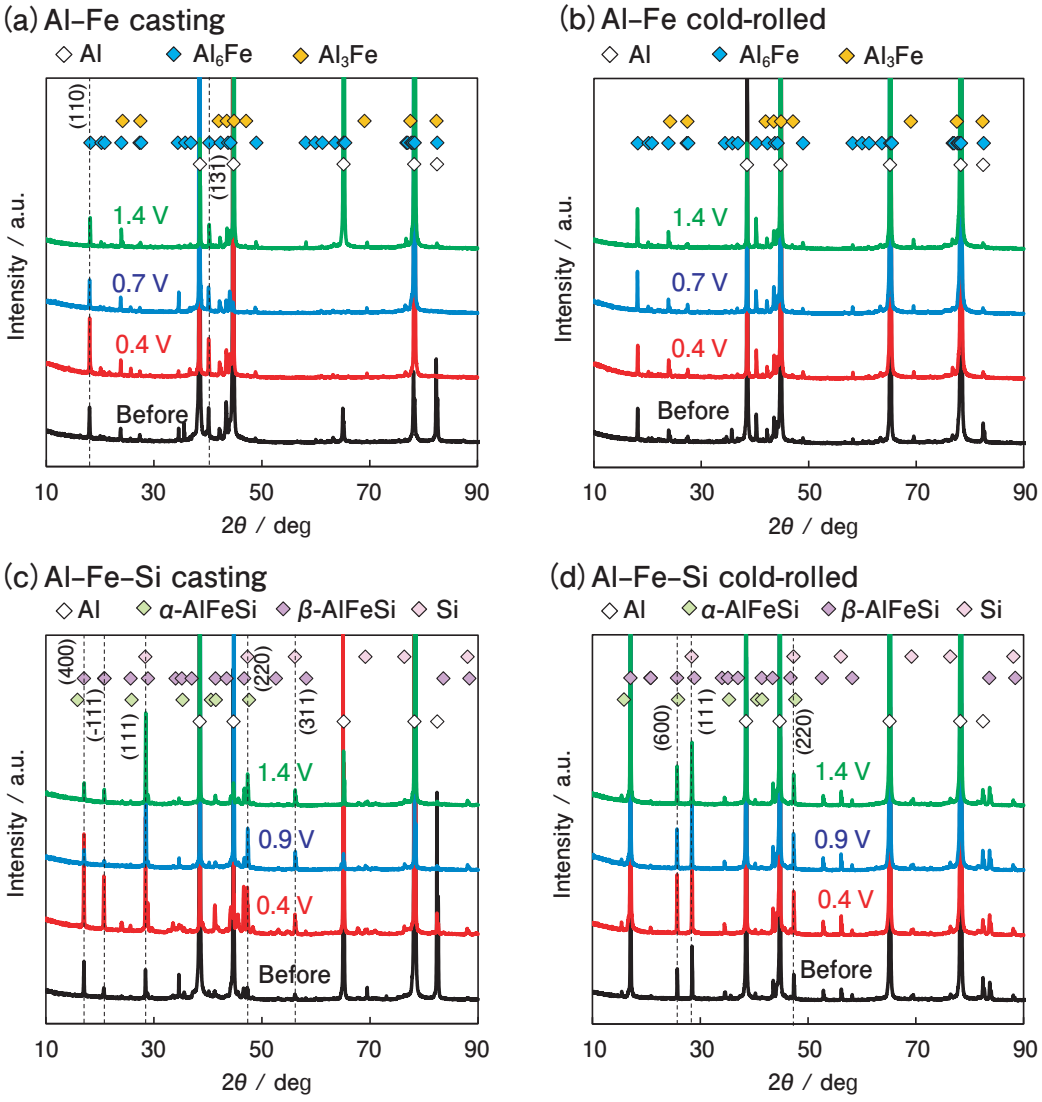

Fig. 4 X-ray diffraction patterns of the Al–1.5%Fe (a) casting alloy and (b) cold-rolled plate and those of the Al–1.5%Fe–3.5%Si (c) casting alloy and (d) cold-rolled plate before and after constant potential electrolysis in the EmImCl–$AlCl_3$ ionic liquid at 0.4, 0.7, 0.9, and 1.4 V, with a charge density of 100 C cm^{-2} at 323 K.

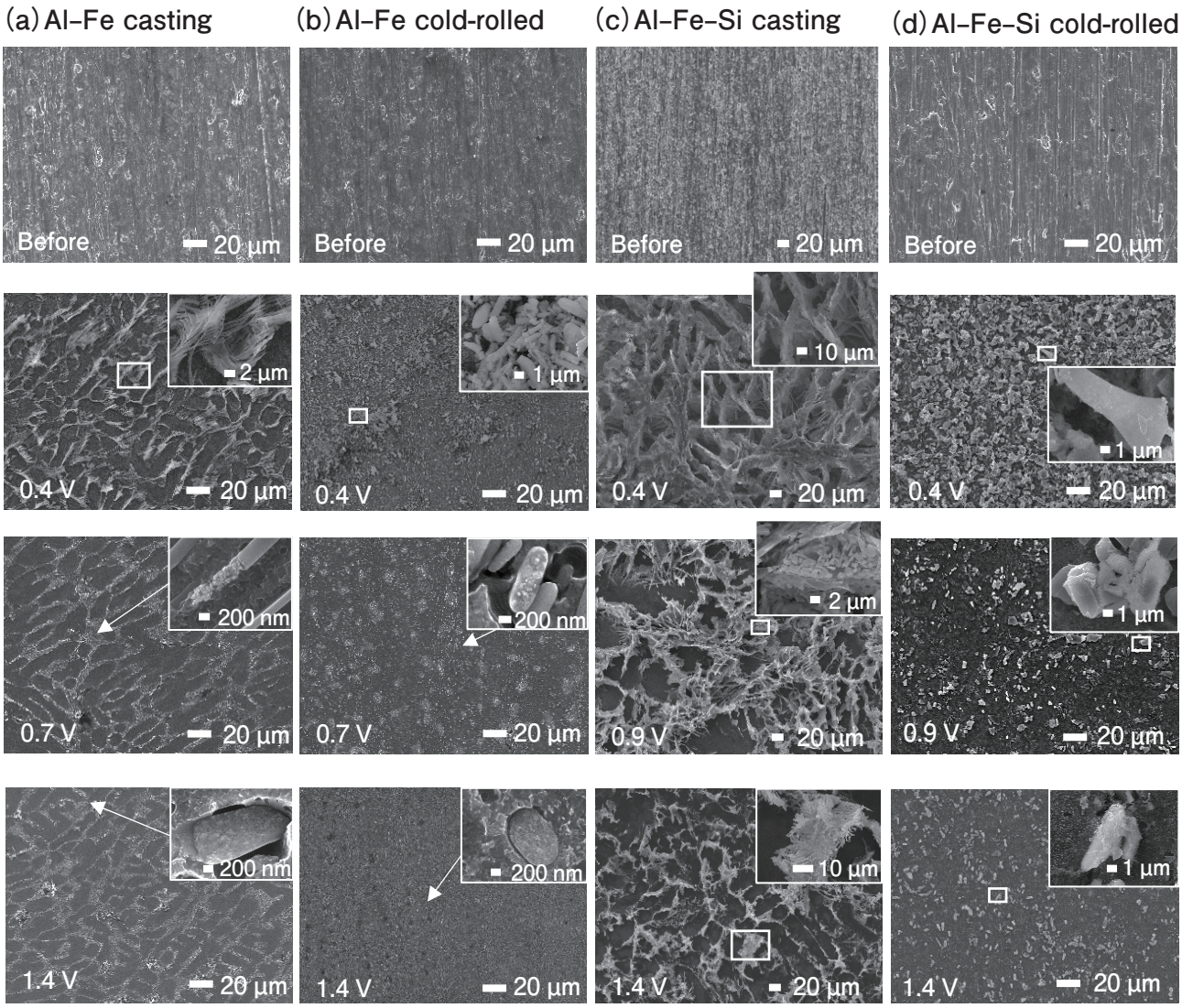

Fig. 5 Field emission scanning electron microscope (FE-SEM) images of the Al–1.5%Fe (a) casting alloy and (b) cold-rolled plate and those of the Al–1.5%Fe–3.5%Si (c) casting alloy and (d) cold-rolled plate before and after constant potential electrolysis in the EmImCl–$AlCl_3$ ionic liquid at 0.4, 0.7, 0.9, and 1.4 V, with a charge density of 100 C cm^{-2} at 323 K.

observed. However, there was no clear peak at the position where only Al_3Fe and α-AlFeSi were detected. Therefore, we determined that Al_6Fe in Al–Fe alloys and β-AlFeSi in Al–Fe–Si alloy were mainly presented from the XRD results. In the XRD diffraction pattern of the Al–1.5%Fe casting alloy (Fig. 4 (a)), the peak intensities of the (110) and (131) planes of Al_6Fe at 0.4 V increased significantly from those before electrolysis, and the peak intensities at 0.7 and 1.4 V were comparable to those before electrolysis. In the XRD diffraction pattern of the Al–1.5%Fe–3.5%Si casting alloy (Fig. 4 (c)), the peak intensities of the (400) and (−111) planes of β-AlFeSi and the (111), (220), and (311) planes of Si at 0.4 V were significantly higher than those before electrolysis. At 0.7 and 1.4 V, the diffraction peak intensities of the (400) and (− 111) planes of β-AlFeSi decreased and remained constant, respectively, to those before electrolysis. However, the peak intensities of the (111), (220), and (311) planes of Si increased from those before electrolysis. In the XRD diffraction pattern (Fig. 4 (d)) of the Al–1.5%Fe–3.5%Si cold-rolled plate, the peak intensities of the (600) plane of β-AlFeSi and the (111) and (220) planes of Si at 0.4 V increased significantly from those before electrolysis. However, at 0.7 and 1.4 V, the peak intensity of the (600) plane of β-AlFeSi remained identical to that before electrolysis, but the peak intensities corresponding to the (111) and (220) planes of β-AlFeSi increased from those before electrolysis.

The FE-SEM images of the anode surfaces after constant potential electrolysis are shown in **Fig. 5**. At 0.4 V, a coarse microstructure was observed on the

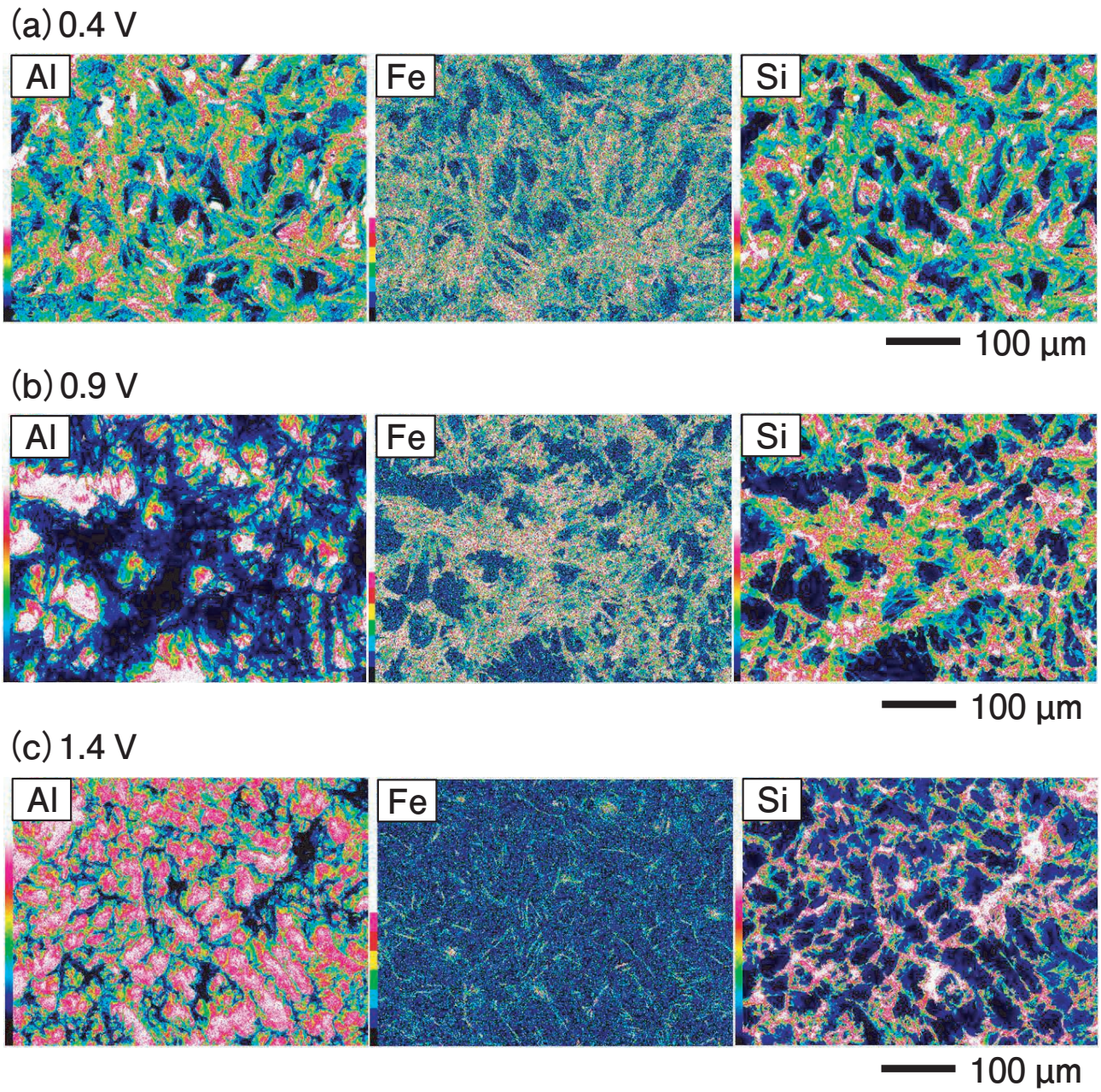

Fig. 6 Energy dispersive spectroscopy (EDS) mapping of Al, Fe, and Si in the Al–1.5%Fe–3.5%Si casting alloy obtained after constant potential electrolysis in the EmImCl–$AlCl_3$ ionic liquid at 0.4, 0.9, and 1.4 V, with a charge density of 100 C cm^{-2} at 323 K.

surface of the Al–1.5%Fe casting alloy (Fig. 5 (a)). At 0.7 and 1.4 V, the coarse microstructures dissolved. At 0.4 V, particles with diameters of a few micrometers were observed to segregate on the surface of the cold-rolled Al–1.5%Fe plate in the form of islands (Fig. 5 (b)). At 0.7 and 1.4 V, these particles dissolved to form a smooth surface. At 0.4 V, a coarse microstructure was observed on the surface of the surface of the Al–1.5%Fe–3.5%Si casting alloy (Fig. 5 (c)). At 0.9 and 1.4 V, these coarse structures dissolved to form an uneven surface. At 0.4 V, particles with diameters of a few micrometers were observed on the surface of the Al–1.5%Fe–3.5%Si cold-rolled plate (Fig. 5 (d)), particles with diameters of a few µm were observed all over the surface. At 0.9 and 1.4 V, these particles dissolved to form an uneven surface.

The EDS mapping of the Al–1.5%Fe–3.5%Si casting alloy surface observed in Fig. 5 is shown in **Fig. 6**. At 0.4 V, Al, Fe, and Si were detected in the coarse surface structure at 0.4 V (Fig. 6 (a)), Fe and Si were detected in the coarse surface structure at 0.9 V (Fig. 6 (b)), and only Si was detected at 1.4 V (Fig. 6 (c)). The EDS mapping of the cross-section of the Al–1.5%Fe–3.5%Si casting alloy after constant

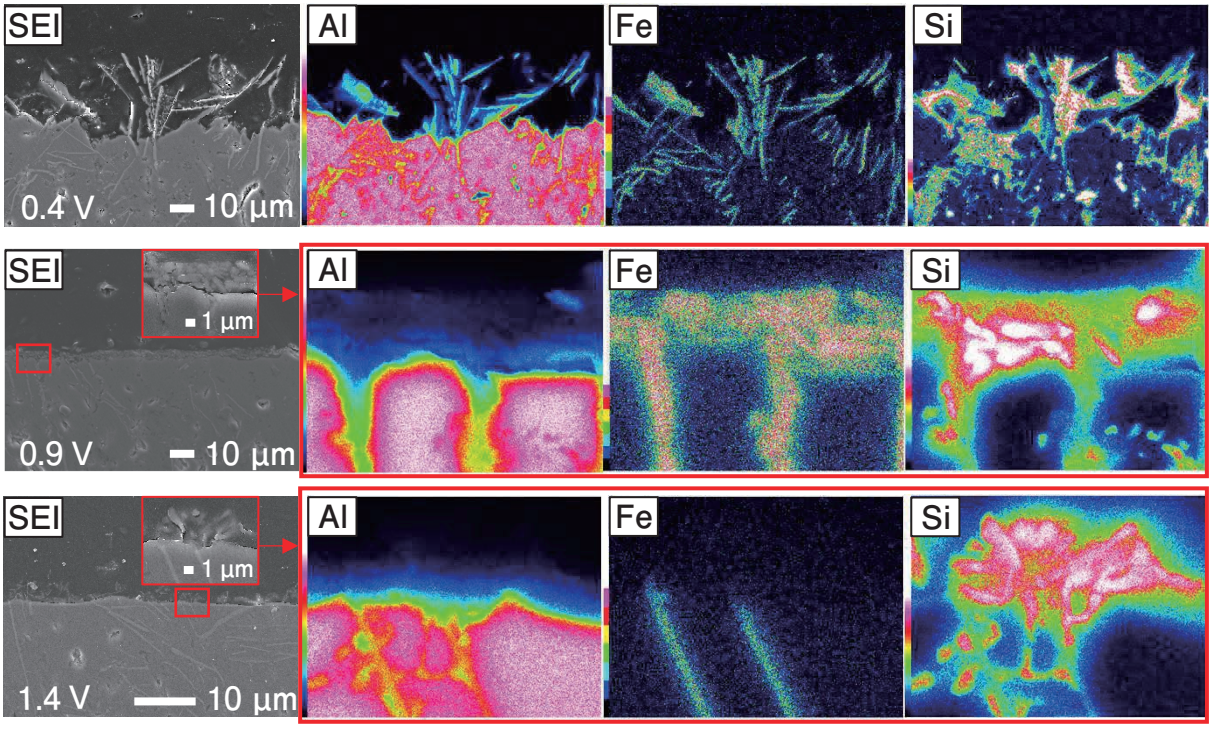

Fig. 7 FE-SEM images and the corresponding Al, Fe, and Si EDS profiles of the cross-sections of the Al–1.5%Fe–3.5%Si casting alloy after constant potential electrolysis in the EmImCl–$AlCl_3$ ionic liquid at 0.4, 0.9, and 1.4 V, with a charge density of 100 C cm^{-2} at 323 K.

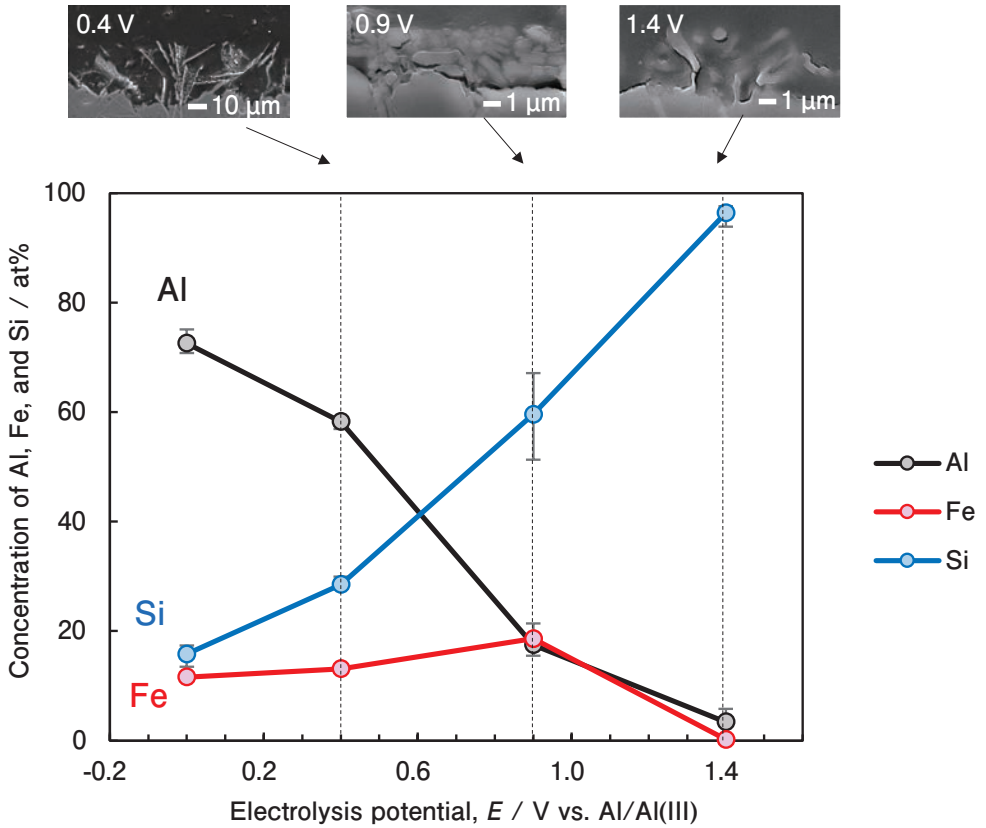

Fig. 8 Al, Fe, and Si concentrations of β-AlFeSi in the Al–1.5%Fe–3.5%Si casting alloy anode surfaces estimated using EDS profiles obtained before and after constant potential electrolysis in the EmImCl–$AlCl_3$ ionic liquid at 0.4, 0.9, and 1.4 V, with a charge density of 100 C cm^{-2} at 323 K.

potential electrolysis is shown in **Fig. 7**. Similar to the surface observation results, Al, Fe, and Si were detected in the coarse structure at 0.4 V, Fe and Si were detected at 0.9 V, and only Si was detected at

1.4 V. The Al, Fe, and Si concentrations of β-AlFeSi on the coarse surface layers of the Al–1.5%Fe–3.5%Si casting alloy anode surfaces estimated from their EDS profiles are shown in **Fig. 8**. The averages of triplicate measurements for each potential were considered for the concentrations. The sum of Al, Fe, and Si was calculated as 100at%. Al concentration decreased with increasing potential, and Si concentration increased with increasing potential. However, Fe concentration increased gradually up to 0.9 V but decreased significantly at 1.4 V.

The Fe and Si concentrations of the anode surfaces and electrodeposits on the cathode before and after constant potential electrolysis are shown in **Fig. 9** and **Table 3**. The Fe and Si concentrations were calculated the sum of Al, Fe, and Si detected by EDS as 100mass%. The anode surface was analyzed at three locations in the EDS analysis, and the average was considered for the Fe and Si concentrations. The electrodeposits on the cathode were analyzed at five arbitrary points in EDS analysis, and the average of the five points was considered for the Fe concentration. For the Al–1.5%Fe casting alloy (Fig. 9 (a)) at 0.4 V, the concentration of Fe on the anode surface increased compared to that before electrolysis, but Fe was not detected in the electrodeposit. At 0.7 and 1.4 V, the Fe concentration on the anode surface was similar to that before electrolysis, but 0.2 and 0.4mass%Fe were detected in the electrodeposits at 0.7 and 1.4 V, respectively. For

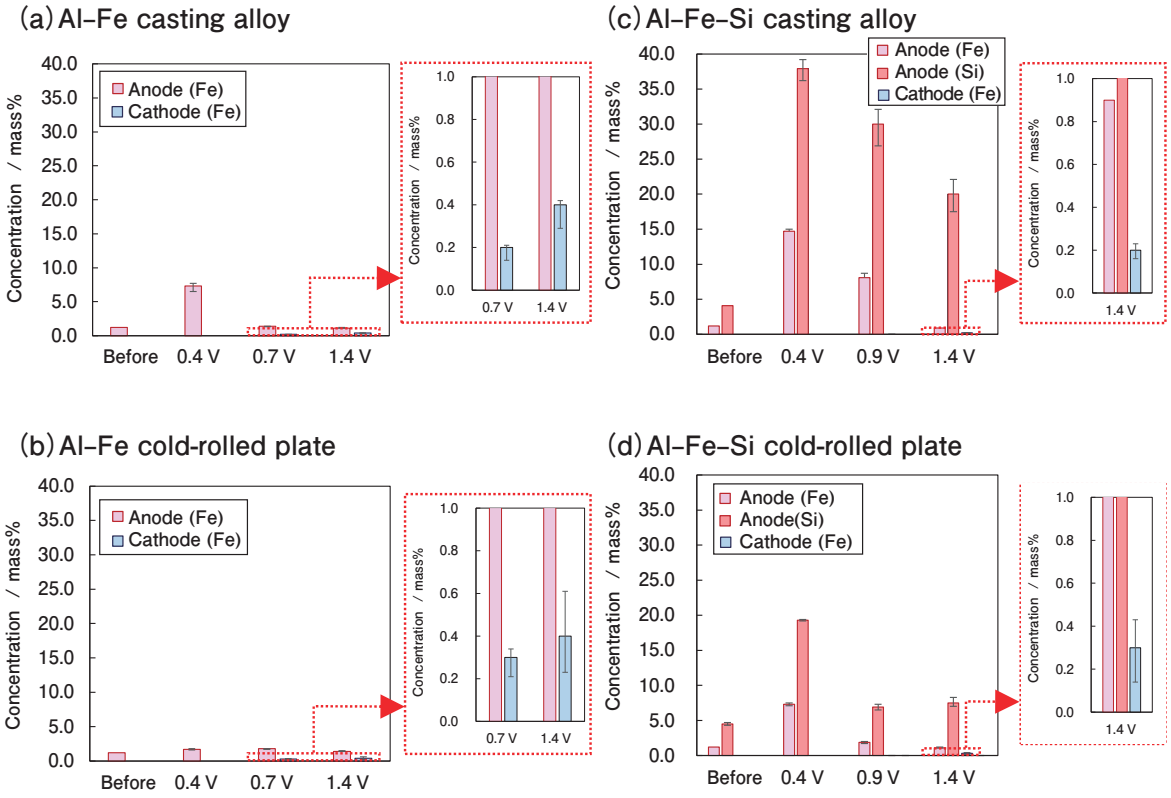

Fig. 9 Fe and Si concentrations in the Al–1.5%Fe (a) casting alloy and (b) cold-rolled plate and the Al–1.5%Fe–3.5%Si (c) casting alloy and (d) cold-rolled plate anode surfaces and the corresponding electrodeposits on the cathode before and after the constant potential electrolysis in the EmImCl–$AlCl_3$ ionic liquid at 0.4, 0.7, 0.9, and 1.4 V, with a charge density of 100 C cm^{-2} at 323 K estimated via EDS.

Table 3 Fe and Si concentrations in anode alloys and electrodeposits on the cathode before and after constant potential electrolysis in the EmImCl–$AlCl_3$ ionic liquid at 0.4, 0.7, 0.9, and 1.4 V with a charge density of 100 C cm^{-2} and at 323 K.

Potential [V vs. Al/Al(III)]	Fe [mass%]		Fe : Si [mass%]	
	Al–Fe (casting)	Al–Fe (cold-rolled)	Al–Fe–Si (casting)	Al–Fe–Si (cold-rolled)
0.4	0.0	0.0	0.0 : 0.0	0.0 : 0.0
0.7	0.2	0.3	—	—
0.9	—	—	0.0 : 0.0	0.0 : 0.0
1.4	0.4	0.4	0.2 : 0.0	0.3 : 0.0

the Al–1.5%Fe cold-rolled plate (Fig. 9 (b)), the Fe concentration on the anode surface was similar before and after electrolysis, but 0.3 and 0.4mass%Fe were detected in the electrodeposit at 0.7 and 1.4 V, respectively. For the Al–1.5%Fe–3.5%Si casting alloy (Fig. 9 (c)) at 0.4 V, the concentrations of Fe and Si on the anode surface were higher than those before electrolysis, but Fe or Si were not detected in the electrodeposit. The concentrations of Fe and Si on the anode surface were lower at 0.9 V than at 0.4 V, but Fe and Si were not detected in the electrodeposit. The concentrations of Fe and Si on the anode surface were lower at 1.4 V than at 0.9 V, but 0.2mass%Fe was detected in the electrodeposits. For the Al–1.5%Fe–3.5%Si cold-rolled plate (Fig. 9 (d)) at 0.4 V, the concentrations of Fe and Si on the anode surface were higher than those before electrolysis, but Fe and Si were not detected in the electrodeposit. The Fe and Si concentrations on the anode surface were lower at 0.9 V than at 0.4 V, but Fe and Si were not detected in the electrodeposit. The Fe concentration on the anode surface at 1.4 V was comparable to that before electrolysis, whereas the Si concentration at 1.4 V was comparable to that at 0.9 V, but 0.3mass%Fe was detected in the electrodeposit

4. Discussion

Pure Al exhibited typical anodic polarization and dissolution behavior in the EmImCl–$AlCl_3$ ionic liquid (Fig. 1)[42]. However, the anodic polarization curves of Al–1.5%Fe and Al–1.5%Fe–3.5%Si anode in the anode polarization curve corresponds to Al_6Fe, and the current density peaks at 0.9 and 1.4 V for the Al–1.5%Fe–3.5%Si alloy anode are attributed to β-AlFeSi. The SEM images of the anode surfaces after constant potential electrolysis exhibited coarse microstructures in the casting alloy and particles with diameters of several micrometers in the cold-rolled plates (Fig. 5). Al and Fe were detected in these microstructures and particles of Al–1.5%Fe, whereas Al, Fe, and Si were detected in Al–1.5%Fe–3.5%Si via EDS mapping. The concentration of these intermetallic compounds were (86.9–88.4) at%Al–(11.6–13.1) at%Fe and (70.8–75.1) at%Al–(11.0–11.8) at%Fe–(13.5–16.6) at%Si. Therefore, these microstructures and particles were considered Al_6Fe and β-AlFeSi ($Al_9Fe_2Si_2$). The XRD peak intensities of Al_6Fe and β-AlFeSi increased at 0.4 V. The XRD peak intensities of Al_6Fe and β-AlFeSi were similar to those before electrolysis at more than 0.7 and 0.9 V, respectively. The SEM images also showed that Al_6Fe was exposed on the surface layer at 0.4 V and dissolved above 0.7 V. This behavior is consistent with the anodic polarization behavior and the change in the XRD pattern with changing applied potential. β-AlFeSi was exposed on the surface layer at 0.4 V and dissolved above 0.9 V. EDS analysis of the Al–1.5%Fe–3.5%Si casting alloy anode surface and cross-section after constant potential electrolysis (Figs. 6–8) shows that the Al concentration in β-AlFeSi decreased, whereas the Fe and Si concentrations increased at 0.9 V, and the Al and Fe concentrations decreased and the Si concentration increased at 1.4 V. This suggests that β-AlFeSi preferentially dissolves Al at 0.9 V, Al and Fe at 1.4 V, and Si is not dissolved at any potential. This behavior is consistent with the anodic polarization behavior and the change in the XRD pattern with changing applied potential. The anode surface of Al–1.5%Fe at 0.4 V after constant potential electrolysis changed to a dark color because of the presence of Al_6Fe on the surface layer (Fig. 3). In the case of Al–1.5%Fe–3.5% Si at 0.4 V, the darkening of the surface is attributed to the presence of β-AlFeSi on the surface layer. The SEM images confirmed the dissolution of Al_6Fe and surface smoothing of Al_6Fe above 0.7 V, suggesting that the higher the potential, the more the Al matrix and Al_6Fe were forced to dissolve at the same rate and the more the surface smoothing was promoted. In the case of Al–1.5%Fe–3.5%Si, the darkening of the surface is attributed to the presence of β-AlFeSi on the surface layer at 0.4 V. The presence of coarser β-AlFeSi in the casting alloy than in the cold-rolled plate could be responsible for the highly uneven surface, although the dissolution of β-AlFeSi proceeded at a noble potential. This difference in the surface conditions could have contributed to a darker surface color of the casting alloy than that of the cold-rolled plates.

As mentioned above, the anodic dissolution behaviors of Al_6Fe and β-AlFeSi were not the same.

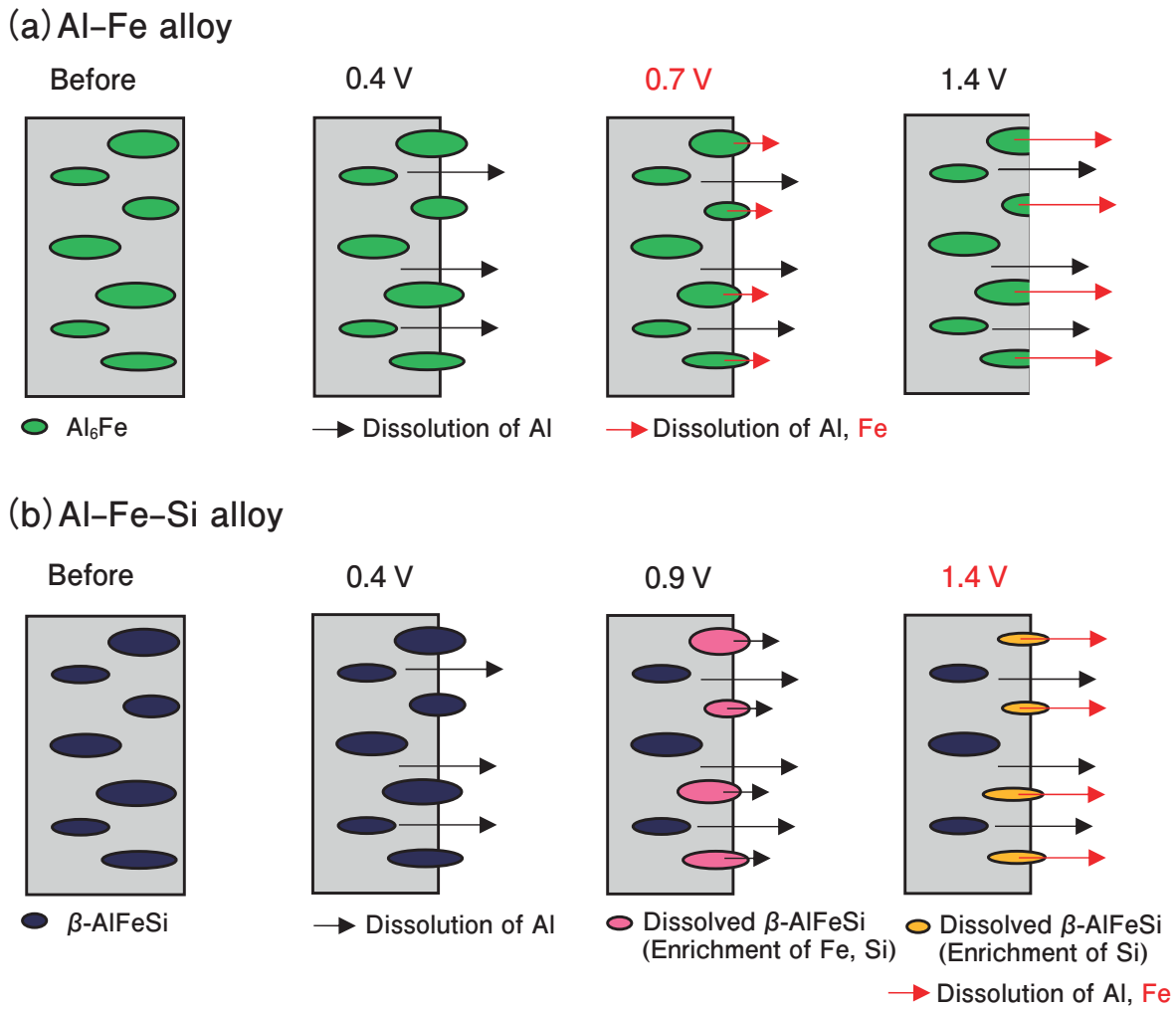

Fig. 10 Schematics of the anodic dissolution of (a) Al–Fe and (b) Al–Fe–Si alloy anodes in the EmIm–$AlCl_3$ ionic liquid.

The anodic oxidation behavior in an aqueous sulfuric acid solution changes depending on the type of intermetallic compound[43), 44)]. Al_6Fe is preferentially oxidized by Al in the early stage of anodization, and an enriched layer of Fe is formed at the interface between Al_6Fe and the anodized film on Al_6Fe. The anodization rate of Al_6Fe is lower than that of the Al matrix[45), 46)]. Si and β-AlFeSi are not easily anodized and are incorporated directly into the anodized film[44), 47), 48)]. In the $AlCl_3$–based electrolyte used in this study, pure Al and pure Fe were anodically dissolved (Fig. 1); however, Si was not easily dissolved[24)]. Si is considered to have low conductivity in low temperature $AlCl_3$–based electrolyte and difficult to dissolve. Since preferential dissolution of Al and Fe was observed in Fig. 8, it was considered the behavior of Si in β-AlFeSi, as well as the Si precipitated in Al–Si alloy[24)], was not easily dissolved in$AlCl_3$–based electrolytes. Furthermore, the anodic dissolution of β-AlFeSi was not as rapid as that of Al_6Fe. Similar to the changes in the anodizing behavior in an aqueous sulfuric acid solution, the anodic dissolution behavior in the $AlCl_3$–based electrolyte may have changed. β-AlFeSi containing Si, which is less dissolvable, could have transformed into an intermetallic compound that is less anode dissolvable than Al_6Fe. A schematic of the anodic dissolution behavior of Al–Fe and Al–Fe–Si alloys is shown in **Fig. 10**.

Analysis of Fe concentration in the cathodic electrodeposit after constant potential electrolysis using Al–1.5%Fe anodes (Fig. 9 (a), (b)) shows that Fe was not detected in the electrodeposit at 0.4 V. However, Fe was detected in the electrodeposit at 0.7 and 1.4 V. This is attributed to the dissolution of Al_6Fe at potentials higher than 0.7 V. The Fe content could have originated from the dissolution of Al_6Fe at the anode and its co-deposition with Al at the cathode. As mentioned above, Al_6Fe is dissolved faster at 1.4 V than at 0.7 V. Therefore, the amount of

Fe ions accumulated in the ionic liquid increases. Therefore, the Fe concentration in the electrodeposit was higher at 1.4 V than at 0.7 V due to an increase in the amount of Fe co-deposited with Al. Analysis of the Fe and Si concentrations in the cathodic electrodeposit after constant potential electrolysis using an Al–1.5%Fe–3.5%Si anode (Fig. 9 (c), (d)) showed that only Fe was detected in the deposit at 1.4 V and Si was not detected in any of the electrodeposits. This is attributed to the dissolution of Fe from β-AlFeSi at 1.4 V. The Fe originated from β-AlFeSi dissolved from the anode and is co-deposited with Al on the cathode. The Si in β-AlFeSi, as well as the Si precipitated in Al–Si alloy[24], is difficult to dissolve in $AlCl_3$–based electrolytes. Therefore, Si was not detected in the electrodeposit at any potential. Furthermore, the analysis of Fe and Si concentrations on the Al–1.5%Fe–3.5%Si anode surface after constant potential electrolysis (Fig. 9 (c), (d)) showed that the maximum Si and Fe concentrations were observed at 0.4 V. The EDS surface analysis of the anode surface after constant potential electrolysis (Fig. 6) showed that β-AlFeSi was observed on the entire anode surface at 0.4 V; however, dissolution of Al or Fe from β-AlFeSi above 0.9 V exposed the matrix surface, resulting in higher Al concentrations and lower β-AlFeSi concentrations. Therefore, the maximum Fe and Si concentrations on the anode surface are observed at 0.4 V (Fig. 9 (c), (d)). In Fig. 9 (c), (d), "Anode (Fe)" at 0.9 V and 1.4 V is much different between casting and cold-rolled plate. Al–Fe–Si casting alloy was observed coarser β-AlFeSi than the cold-rolled plate in Fig. 5. Since the anode surfaces were evaluated by EDS mapping analysis, it was assumed that more Fe was detected in casting alloy with enriched β-AlFeSi at the surface than in the cold-rolled plates.

These results reveal that the anodic dissolution behavior of the metallurgical structure of Al–Fe and Al–Fe–Si alloys in EmImCl–$AlCl_3$ ionic liquid depends on the applied potential. The dissolution of Fe in Al_6Fe of the Al–Fe alloy in the electrolyte was suppressed by controlling the anodic dissolution potential. In the case of β-AlFeSi, the potential at which Fe dissolves from the intermetallic compound shifts to the noble potential, resulting in a metallographic structure that is difficult to dissolve in the electrolyte. This contributes to the purity of the electrorefined Al because control of the anodic dissolution potential and metallurgical structure suppresses the dissolution of Fe in the intermetallic compound into the electrolyte. In this study, EDS was used to analyze the purity of electrorefined Al. Since detection limit of the element by EDS is approximately 0.1mass%, it is assumed that electrorefined Al of more than 99.9% could be obtained in this study.

5. Conclusion

The anodic dissolution and cathodic electrodeposition behaviors of Al–Fe and Al–Fe–Si alloys in EmImCl–$AlCl_3$ ionic liquid (molar ratio = 1 : 2) were investigated in this study to clarify the optimal electrorefining conditions for obtaining high-purity Al at the cathode. Anodic polarization curves, constant potential electrolysis, XRD, SEM, FE-SEM, and EDS were used to study the anode surfaces, cross-sections, and the cathode electrodeposits.

Al–Fe alloys showed an anodic current density peak corresponding to Al_6Fe at approximately 0.7 V vs Al/Al(III), and Al–Fe–Si alloys showed a peak corresponding to β-AlFeSi at approximately 0.9 and 1.4 V. Furthermore, the casting alloy and the cold-rolled alloy showed different electrochemical behavior at the boundary of 0.4 V, and changes of the anodic polarization behavior were considered to be related to the electrical conductivities of alloys, and formation process and thickness of the solidified electrolyte layer.

In the case of β-AlFeSi, Al dissolved preferentially at 0.9 V, Al and Fe at 1.4 V, and Si did not dissolve at any applied potential. Additionally, enrichment of coarse β-AlFeSi at the surface of casting alloy was observed.

At potentials where Fe dissolves from Al_6Fe or β-AlFeSi, Fe was co-deposited with Al on the cathode.

In the case of the Al–Fe–Si alloy, the dissolution of Fe in the electrolyte was suppressed because β-AlFeSi, which has a higher dissolution starting potential than Al_6Fe, was formed, and high-purity Al was deposited at the cathode.

Our findings suggest that Al alloys with β-AlFeSi intermetallic compounds that are less likely to dissolve Fe at the anode are optimal for obtaining more than 99.9% of high-purity Al from Al alloys containing Fe in the electrorefining method.

Acknowledgments

This study was partially supported by the New Energy and Industrial Technology Development Organization (NEDO). We express our gratitude to all concerned parties.

REFERENCES

1) B. Phillion, S. Thompson, S.L. Cockcroft and M.A. Wells: Mater. Sci. Eng. A, **497** (2008), 388-394.
2) W. Wen, Y. Zhao and J.G. Morris: Mater. Sci. Eng. A, **392** (2005), 136-144.
3) D.M. Jiang, S.B. Kang and H.W. Kim: Mater. Sci. Technol., **15** (1999), 1401-1407.
4) J. Hirsch: Mater. Trans., **52** (2011), 818-824.
5) J. Evertsson, F. Bertram, L. Rullik, G. Harlow and E. Lundgren: J. Electroanal. Chem., **799** (2017), 556-562.
6) H. Kvande and P.A. Drabløs, J. Occup: Environ. Med., **56** (2014), S23-S32.
7) M. Mahinroosta and A. Allahverdi: J. Environ. Manage., **223** (2018), 452-468.
8) G.M. Haarberg: ECS Trans., **98** (2020), 181-187.
9) S. Capuzzi and G. Timelli: Metals, **8** (2018), 249.
10) S.K. Das, W.J. Long, H.W. Hayden, J.A.S. Green and W.H. Hunt: JOM, **56** (2004), 14-17.
11) J. Cui and H. J. Roven: Trans. Nonferrous Met. Soc. China, **20** (2010), 2057-2063.
12) S.K. Das and W. Yin: JOM, **59** (2007), 57-63.
13) A. N. Løvik, R. Modaresi and D.B. Müller: Environ. Sci. Technol., **48** (2014), 4257-4265.
14) A. Gesing and R. Wolanski: JOM, **53** (2001), 21-23.
15) P. R. Goulart et al.: Intermetallics, **17** (2009), 753-761.
16) P.R. Goulart, J.E. Spinelli, N. Cheung and A. Garcia: Mater. Chem. Phys., **119** (2010), 272-278.
17) R. K. Shiue, S. K. Wu and Y. L. Lee: Intermetallics, **13** (2005), 818-826.
18) Z.M. Shi, K. Gao, Y.T. Shi and Y. Wang: Mater. Sci. Eng. A, **632** (2015), 62-71.
19) P. Moldovan, G. Popescu and F. Miculescu: J. Mater. Process. Technol., **153-154** (2004), 408-415.
20) D. Bösch, S. Pogatscher, M. Hummel, W. Fragner, P.J. Uggowitzer, M. Göken and H.W. Höppel: Metall. Mater. Trans. A, **46** (2015), 1035-1045.
21) E. Cinkilic, C.D. Ridgeway, X. Yan and A.A. Luo: Metall. Mater. Trans. A, **50** (2019), 5945-5956.
22) H. Nunes, O. Emadinia, R. Soares, M.F. Vieira and A. Reis: Materials, **16** (2023), 895.
23) H. Hatayama, I. Daigo, Y. Matsuno and Y. Adachi: Resour. Conserv. Recycl., **66** (2012), 8-14.
24) S. Oya, J. Nunomura, H. Matsushima, Y. Kyo, Y. Kojima and M. Ueda: Electrochemistry, **90** (2022), 127001.
25) J. Nunomura, H. Matsushima, Y. Kyo, Y. Kojima and M. Ueda: J. Electrochem. Soc., **169** (2022), 082518.
26) J. Nunomura, H. Matsushima, Y. Kyo, Y. Kojima and M. Ueda: Electrochim. Acta, **460** (2023), 142601.
27) T. Ishikawa, S. Konda and T. Narita: ECS Proc. Vol., **1987-7** (1987), 734-743.
28) V. Schwarz and H. Wendt: J. Appl. Electrochem., **25** (1995), 34-40.
29) M. Ueda, K. Imasawa, S. Konda, T. Sasaki, T. Ishikawa and T. Ohtsuka: Electrochemistry, **67** (1999), 695-699.
30) M. Zhang, V. Kamavarum and R.G. Reddy: JOM, **55** (2003), 54-57.
31) V. Kamavaram, D. Mantha and R. G. Reddy: Electrochim. Acta, **50** (2005), 3286-3295.
32) D. Pradhan and R.G. Reddy: Mater. Chem. Phys., **143** (2014), 564-569.
33) D. Pradhan and R.G. Reddy: Metall. Mater. Trans. B, **43** (2012), 519-531.
34) S.K. Kim and R.G. Reddy: J. Korean Inst. Surf. Eng., **34** (2001), 553-567.
35) B.L. Silva, A. Garcia and J.E. Spinelli: Mater. Lett., **89** (2012), 291-295.
36) S. Onurlu and A. Tekin: J. Mater. Sci., **29** (1994), 1652-1655.
37) S. Zajac, B. Hutchinson, A. Johansson and L.O. Gullman: Mater. Sci. Technol., **10** (1994), 323-333.
38) P. Giridhar, B. Weidenfeller, S.Z.E. Abedin and F. Endres: Phys. Chem. Chem. Phys., **16** (2014), 9317-9326.
39) R.T. Carlin, H.C. De Long, J. Fuller and P.C. Trulove: J. Electrochem. Soc., **145** (1998), 1598-1606.
40) H. Yamamoto, Y. Koma, R. Kishino, A. Nozaki and M. Morishita: J. Electrochem. Soc., **168** (2021), 012503.
41) R. Nadella, D.G. Eskin, Q. Du and L. Katgerman: Prog. Mater Sci., **53** (2008), 421-480.
42) R. Böttcher, A. Ispas and A. Bund: Electrochem. Commun., **115** (2020), 106720.
43) J. Cote, E.E. Howlett, M.J. Wheeler and H.J. Lamb: Plating, **56** (2015), 386-394.
44) J. Cote, E.E. Howlett and H.J. Lamb: Plating, **57** (2015), 484-496.
45) K. Shimizu, G.M. Brown, H. Habazaki, K. Kobayashi, P. Skeldon, G.E. Thompson and G.C. Wood: Corros. Sci., **42** (2000), 831-840.
46) K. Shimizu, G.M. Brown, H. Habazaki, K. Kobayashi, P. Skeldon, G.E. Thompson and G.C. Wood: Corros. Sci., **41** (1999), 1783-1790.
47) G. Scampone and G. Timelli: Adv. Eng. Mater., **24** (2022), 2101480.
48) F. Zhang, J.O. Nilsson and J. Pan: J. Electrochem. Soc., **163** (2016), C609-C618.

Junji Nunomura
Fundamental Research Department,
Research & Development Center,
Marketing & Technology Division,
UACJ Corporation, Dr. Eng.

Hisayoshi Matsushima
Faculty of Engineering, Hokkaido University,
Dr. Eng.

Yoshihiko Kyo
Fundamental Research Department,
Research & Development Center,
Marketing & Technology Division,
UACJ Corporation, Dr. Eng.

Yoichi Kojima
Research & Development Center,
Marketing & Technology Division,
UACJ Corporation, Ph. D.

Mikito Ueda
Faculty of Engineering, Hokkaido University,
Ph. D.